communications materials

A Nature Portfolio journal

Article

Article in Press

https://doi.org/10.1038/s43246-026-01418-0

Mechanisms of $\beta \leftrightarrow \gamma$ transformations in tin induce asymmetric kinetics

Check for updates

Robin Fréville[1,2] ✉, Agnès Dewaele[3,4], Charles Pépin[3,4], Nicolas Bruzy[3,4], Florent Occelli[3,4], Matteo Levantino[2] & Nicolas Guignot[5]

Solid-solid phase transformation mechanisms need to be understood to establish suitable kinetic laws. Here, the β-Sn $\leftrightarrow$ γ-Sn phase transformations are investigated at different strain rates at 300 K. On one side, single crystals have been statically compressed and characterized using in situ x-ray diffraction. Multiple transformation cycles were performed in diamond anvil cells to measure their conditions and the associated microstructures. $(101)_\beta||(110)_\gamma$ and $[10\bar{1}]_\beta||[1\bar{1}1]_\gamma$ orientation relationships (OR) between β-Sn and γ-Sn are observed in most cases, for both direct and reverse transformations. An atomic martensitic transformation mechanism, associated with self-accommodation, is proposed to account for these OR and variant selection. However, γ-Sn $\rightarrow$ β-Sn reversion also presents features that are consistent with recrystallization in β-Sn or a massive transformation. On the other side, time-resolved (22 μ s scale) dynamic diamond anvil cell experiments have been carried out. They show that while β-Sn $\rightarrow$ γ-Sn transformation is fast ($P_{\beta\rightarrow\gamma}$=10.9 $\pm$ 0.2, insensitive to strain rate), reversion pressure $P_{\gamma\rightarrow\beta}$ varies with strain rate, from 9.4 $\pm$ 0.8 GPa to 6.35 $\pm$ 0.7 GPa. Moreover, timescales of β-Sn formation and subsequent recrystallization/growth in this phase can be distinguished. A different kinetic description needs to be used for direct and reverse transitions.

The knowledge of the equilibrium phase diagram of the elements involved is a prerequisite for any science under extreme conditions. Now that volumetric compression rates can be varied by several decades, from 10^{-4} s^{-1} to 10^{9} s^{-1}, with time-resolved in situ measurements, kinetic effects in phase transformation conditions and subsequent effects on measured phase diagrams have been disclosed for several systems. The strain rate dependence of phase transitions exhibits significant material-specific variations. Shock compression regimes, characterized by strain rates exceeding 10^{6} s^{-1}, induce substantial shifts in the α-Fe $\rightarrow$ ϵ-Fe transition pressure, with reported increases of tens of GPa[1]. By comparison, intermediate strain rates ranging from 10^{0} to 10^{2} s^{-1}, readily accessible via dynamic diamond anvil cell experiments[2], produce negligible effects on the phase transition pathway in iron[3]. However, this behavior is not universal: materials such as TiO_2 demonstrate considerably greater strain rate sensitivity, exhibiting measurable transition pressure shifts at strain rates as low as 10^{0} s^{-1} [4,5]. Notably, strain rate effects can yield counterintuitive outcomes: in Sb[6] and Si[7], high strain rates reduce the stability field of intermediate high-pressure phases, whereas in Bi[8] they can suppress these phases altogether. Understanding such different kinetic behaviors requires a description of the transformation mechanism from atomic to mesoscale. Two classes of solid-solid phase transformations are described in the literature. Martensitic transformations have a 'military' displacive atomic mechanism that produces a new phase seed with a time scale that can be as low as sub-ns; however, they induce elastic stresses that need to be relaxed, which is a phenomenon at the microstructure scale. Reconstructive transformations, with nucleation and diffusional growth steps, are thermally activated and slower but produce a microstructure at mechanical equilibrium. Massive transformations constitute a particular class of diffusion-enhanced transformations in which the interface migrates without long-range diffusion, allowing rapid transformation; they can transform polycrystals into single crystals.

Sn (tin) exhibits a rich polymorphism under high pressure and varying temperatures that has been studied with different techniques and platforms. This makes it an archetypal system to study phase transformations in metals and their mechanisms. Under ambient conditions, it adopts a body-centered tetragonal $I4_1/amd$ (β-Sn) structure (4 atoms/unit cell), similar to the high pressure phases of Si and Ge. Above ~ 10.8 GPa, β-Sn transforms to another body-centered tetragonal structure (bct), called γ-Sn (space group: $I4/mmm$, same as In-I, 2 atoms/unit cell), with an initial c/a ratio of ~ 0.91

[1]Karlsruhe Institute of Technology, Institute for Applied Materials, Karlsruhe, Germany. [2]European Synchrotron Radiation Facility, Grenoble, France. [3]CEA, DAM, DIF, Arpajon, France. [4]Université Paris-Saclay, CEA, Laboratoire Matière en Conditions Extrêmes, Bruyères-le-Châtel, France. [5]Synchrotron Soleil, Gif-sur-Yvette Cedex, France. ✉e-mail: robin.freville@esrf.fr

(a_γ=3.694 Å and c_γ=3.370 Å at 10.8 GPa). bco (*Immm*), bcc ($Im-3m$), and hcp ($P63/mmc$)[9,10] phases have been observed at higher pressures, but the present report focuses on β-Sn $\leftrightarrow$ γ-Sn transition.

A volume decrease of ~ 1.9%[10–12] has been measured for the β-Sn $\rightarrow$ γ-Sn transformation, and a hysteresis between the direct and reverse transition pressures of 2-3 GPa is observed under both static[12] and dynamic[11] compressions. A possible martensitic (or displacive, in this report we use the two words equivalently) mechanism at the atomic scale has been suggested by Katzke et al.[13], based on the early work of Musgrave[14]. It involves atomic shuffles of maximum $\pm 3/8c_\gamma$, and a compressive transformation strain (norm 0.15). As far as we know, it has not been validated experimentally, which can be done by measuring the Orientation Relationship (OR) between parent and daughter phases predicted for this mechanism: $(110)_\beta||(100)_\gamma$ and $[001]_\beta||[001]_\gamma$. Katzke mechanism produces a single *variant* for both direct β-Sn $\rightarrow$ γ-Sn and reverse γ-Sn $\rightarrow$ β-Sn transitions. The term variant corresponds to one orientation of a daughter phase, for a fixed orientation of a parent phase[15]. In general, dislocation generation and/or twinning allow releasing the martensitic transformation strain[16]. The 4 known twinning systems described for β-Sn and γ-Sn, or similar phases, that will be used in this work, are described in the Tab. S1 of the Supplementary Materials[17]; the last column of the table indicates how they are noted in this report.

Here, we study $\beta \leftrightarrow \gamma$ phase transformations in tin by static and dynamic compression in diamond anvil cells (DAC). Static in situ measurements of microstructures induced by cycling the transformations in starting single crystals disclose the transition mechanisms involved. Two martensitic mechanisms are observed, but the $\gamma \rightarrow \beta$ transformation also bears diffusive features. $\beta \leftrightarrow \gamma$ transformations, induced by dynamic compression/decompression of multi-grain foils, have also been monitored with time-resolved X-ray diffraction (XRD). Only the reversion pressure exhibits a strain rate effect. The measured microstructural evolution complements the static measurements, evidencing strong recrystallization of β-Sn at the ms time scale, which explains static observations.

Results and discussion

Microstructures observed in static measurements

The static measurements reported here have been carried out using a powder Sn grain (Run 1) and a cold rolled Sn foil (Run 2), annealed to approach a single-crystal state. These samples were cyclically compressed in DACs, under hydrostatic conditions in a helium pressure medium, to induce $\beta-\gamma-\beta$ transformations, characterized with XRD as described in "Methods". Multi-exposure datasets were collected while rotating the DAC around the vertical axis between $-\theta_{max}$ and $+\theta_{max}$ with θ_{step} steps around a vertical axis to measure crystal orientations. TIMELeSS multigrain tools, available from the FABLE project(https://github.com/FABLE-3DXRD/TIMEleSS) are dedicated to this purpose. Fig. 1 shows starting samples and their XRD signal; the weak (ratio $1/10^4$) diffuse signal between main XRD peaks for Run 2 sample is interpreted as a stacking disorder feature. Transformation conditions and Equation of State are detailed in Section S.B of the Supplementary Materials[17]. They are consistent with previous studies, with a direct transformation at 10.9 $\pm$ 0.2 GPa, and a reversion at 9.4 $\pm$ 0.8 GPa (Tab. S2, Fig. S2).

Crystal orientations measured in Run 1 are represented in Fig. 2 as an evolution sketch (a) and pole figures (b-d). Starting from a dominant β_1 orientation (Fig. 1a), three $(101)_\gamma$ twinned orientations (γ_1, γ_2, γ_3) are formed (Fig. 2b). Two ORs are identified: Katzke OR and a second OR defined by $(101)_\beta||(110)_\gamma$ and $[10\bar{1}]_\beta||[1\bar{1}1]_\gamma$, observed between β_1-γ_1 and β_1-γ_3, respectively, within ~ 10° (i.e., inside experimental uncertainty for this run; Fig. 2b, c). To our knowledge, the second OR found here does not correspond to any mechanism described in the literature. We call it hereafter TW (This Work) OR. Upon reversion, a new β-Sn orientation (β_2) forms, with a clear γ_2-β_2 TW OR. It comes as a surprise that three starting γ-Sn orientations produce crystal(s) with a single orientation. This behavior cannot be attributed to a variant selection by memory effect[18], as the new β crystal orientation differs from the starting one. Possible mechanisms include de-twinning in γ-Sn prior to the phase transformation or atomic diffusion in β-Sn or γ-Sn. An additional $\beta \rightarrow \gamma \rightarrow \beta$ cycle has been performed during Run 1. During this cycle, three γ-Sn orientations (γ_4, γ_5, and γ_6) are produced, all related to β_2 with TW OR (see Fig. S5 of the Supplementary[17]). The reversion restores the crystal back to β_2 orientation.

In Run 2, one grain β_A, with an XRD signal as presented in Fig. 1b, is present throughout most of the starting sample. Additional grains are observed close to its edges and are not followed. At 11.0 GPa, four γ-Sn orientations (γ_A to γ_D) form, with OR summarized in Fig. 3. TW OR is found three times, the fourth orientation being obtained by subsequent $(101)_\gamma$ twinning (see definitions in Tab. S1[17]). Only one orientation β_B, forms during $\gamma \rightarrow \beta$ reversion from four γ-Sn orientations, and accurate TW OR exists between γ_B and β_B. Again, de-twinning of γ-Sn could explain this, but the decrease in crystal mosaicity (Supplementary Fig. S3[17]) and the decrease of the diffuse signal between main XRD peaks observed in β_A suggest that atomic diffusion was at play to heal it. Atomic diffusion processes are thermally activated and competitive with respect to displacive mechanisms when $T > T_{melt} \times 0.4$[19]. This is the case here at 9 GPa and 300 K, with an extrapolated melting temperature of β-Sn around 700 K. These mechanisms include recrystallization in β-Sn after phase transformation, where the crystal of β_B-Sn would grow to cover the entire sample, this recrystallization being induced by transformational stress. Alternatively, one crystal of β-Sn could have formed massively from γ-Sn. Massive mechanisms for solid-solid phase transformation involve nucleation and growth by atomic diffusion steps; they can transform polycrystals into single crystals, as observed here. OR can be reported for massive transformations when the starting nucleus forms with a displacive mechanism, leading to a coherent boundary[19].

In run 2, three additional full $\beta \rightarrow \gamma \rightarrow \beta$ cycles and one compression are performed after the first cycle. Cycle 2 reversion forms a new single crystal (β_C), which is recovered in subsequent cycles. It is interesting to note that β_C orientation has the $\vec{a}$ axis aligned with the direction of compression. The direct transitions produce a more complex microstructure with two main γ-Sn orientations, which becomes reproducible after the fourth cycle. TW OR is systematically observed, with a $(112)_\gamma$ twinning relationship between two variants (see Fig. 3a–c).

To sum up, β-Sn $\rightarrow$ γ-Sn $\rightarrow$ β-Sn transformations exhibit a displacive character as OR are observed between parent and child phases: once in Run 1, Katzke OR; several times in both runs, a new OR called TW. Katzke displacive mechanism—which has only one variant and a uniaxial compressive strain tensor[13]—is coupled with $(101)_\gamma$ twinning, which likely releases transformation stress. The repeated observation of TW OR, for most of the transformation cycles in both samples, regardless of their starting shape and microstructure, indicates that it is a likely dominant mechanism. After β-Sn $\rightarrow$ γ-Sn transformation, two γ-Sn TW variants repeatedly coexist, but neither plastic strain nor $(101)_\gamma$ twinning are observed. The $\gamma \rightarrow \beta$ transformation exhibits strong diffusive features (crystal growth and a decrease in mosaicity), even if TW OR is systematically observed.

Below, we discuss how observed TW OR and variant selection can be interpreted by an atomistic martensitic mechanism.

$\beta \leftrightarrow \gamma$ martensitic mechanisms

Vigilano software[20] has been used to determine if TW OR could result from the Katzke mechanism[13] coupled with twinning. All occurrences of TW OR have been compared (in terms of misorientation angles) to sequences including the Katzke mechanism and up to two twinning steps (listed in Tab. S1[17]). When double twinning of one phase is involved, the hypothesis is made that the same twinning system is activated at both steps; as recently observed in ϵ-Fe[21] and γ-Fe[18]. The results (tabulated in Tab. S6[17]) show that Katzke mechanism has to be coupled with at least two twinnings to reproduce the observed OR $\beta \xrightarrow[(301)\beta]{\text{Twinning}} \beta' \xrightarrow[(301)\beta]{\text{Twinning}} \beta'' \xrightarrow{\text{Katzke}} \gamma$ and $\beta \xrightarrow[(101)\beta]{\text{Twinning}} \beta' \xrightarrow[(101)\beta]{\text{Twinning}} \beta'' \xrightarrow{\text{Katzke}} \gamma$ (or reverse). If the system follows such paths, it is

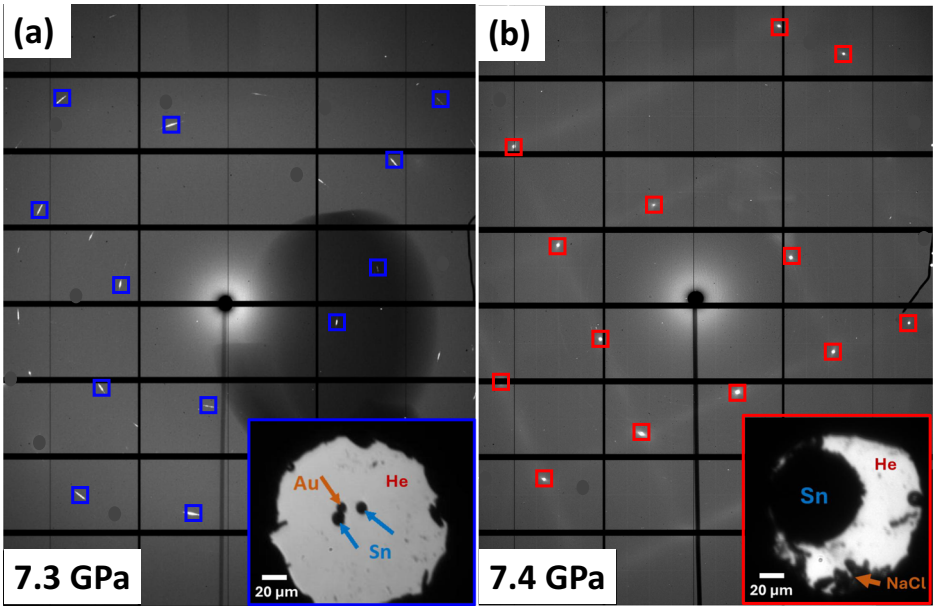


Fig. 1 | Composite diffraction images of starting samples. a Run 1 (powder grain) at 7.3 GPa, and **b** Run 2 (annealed foil) at 7.4 GPa. Blue/red square boxes indicate the position of XRD peaks for β_1/β_A single crystals (see text). The insets show pictures of the high-pressure chambers.

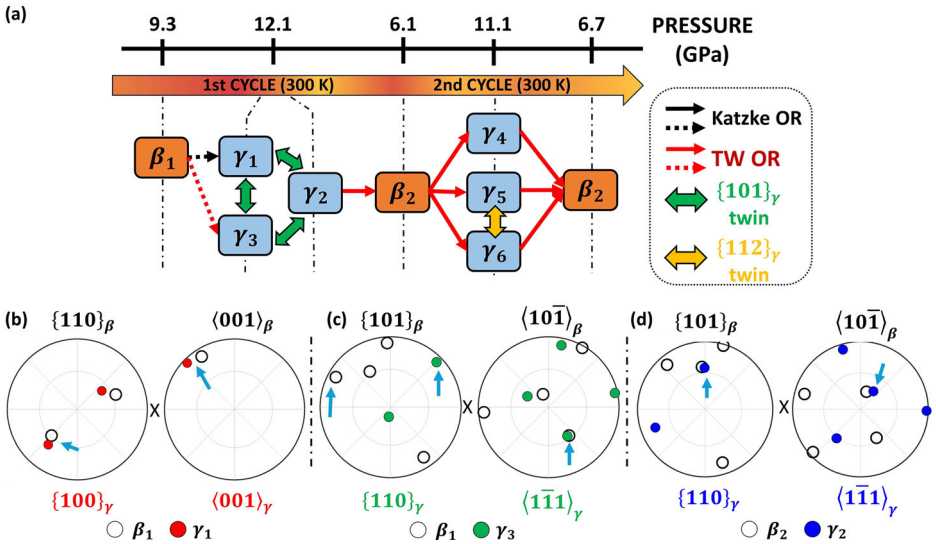


Fig. 2 | Run 1. a Schematic representation of orientations and OR. This work (TW) OR is $(101)_\beta||(110)_\gamma$ and $[10\bar{1}]_\beta||[1\bar{1}1]_\gamma$. Plain/dashed arrows indicate that OR are observed within 2 °/10 ° (see computations in Tab. S6[17]). **b** Pole figure showing Katzke OR between β_1 (empty black circles) and γ_1 (red dots). **c** Pole figure showing TW OR between β_1 (empty black circles) and γ_3 (green dots). In both cases the observed OR present a mis-orientation of ~ 10° compared to the perfect ones. **d** Pole figure showing TW OR between γ_2 (blue dots) and β_2 (empty circles). Blue arrows highlight the coincidences. X (horizontal) is the compression direction.

surprising that Katzke OR alone is observed only seldom in our experiments. We thus believe that TW OR are not likely to be explained by Katzke mechanism, and consider below an alternative atomistic mechanism.

The atomistic mechanism involved in TW OR is represented in Fig. 4: a $(101)_\beta$ plane must transform into a $(110)_\gamma$ plane; such transformation produces 8 variants, as four equivalent $(101)_\beta$ planes and two different $(110)_\gamma$ planes exist. The transformation requires small atomic shuffles, illustrated in Fig. 4a: a vertical translation of the four atoms located within the faces of the conventional double bct unit cell forms the sets of four atoms that outline the future $(110)_\gamma$ pattern. To obtain the required γ-Sn lengths and angles, an additional deformation is required: see Fig. 4c.

The deformation gradient F for this transformation, defined by $F = I + \nabla u$, where I is the identity of second-order tensors and ∇u is the spatial gradient of displacement, is evaluated in section S.I of the Supplementary Materials[17]. It is:

$$F = \begin{bmatrix} 1.06 & 0.40 & 0.15 \\ 0.25 & 1.02 & 0.47 \\ -0.04 & -0.22 & 0.90 \end{bmatrix}. \quad (1)$$

$\frac{1}{2}(F^T F - I)$ is 0.64. A zero norm would correspond to an absence of macroscopic strain; 0.64 is a high value, significantly larger than for Katzke mechanism (0.15), that would imply large elastic stresses in the material during the transformation. However, pairs of γ-Sn variants sharing a $(112)_\gamma$ plane are systematically formed (see Figs. 2a, 3a); they correspond to variants V1 and V2 listed in Tab. S5 of the Supplementary Materials[17]. This pairing greatly releases transformation strain: the strain calculated for such pairs of the same size has a magnitude of only 0.104. This is called *self-accommodation* in shape-memory alloys, where the variants of martensite arrange themselves in such a manner that there is no macroscopic change in shape[22]. By similarity with these materials, we can imagine a so-called

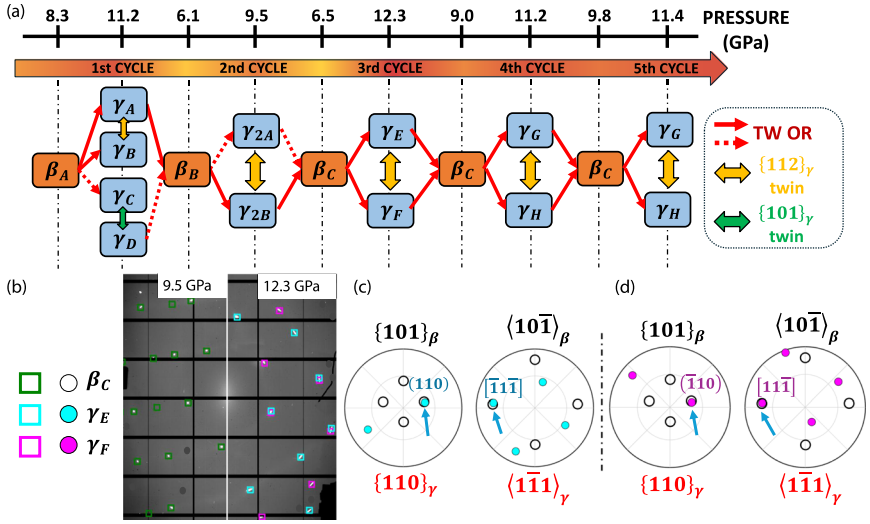


Fig. 3 | Run 2. a Schematic representation of orientations and OR during the experiment. This work (TW) OR is $(101)_\beta||(110)_\gamma$ and $[10\bar{1}]_\beta||[1\bar{1}1]_\gamma$. Plain/dashed arrows indicate that OR are observed within 2 °/10 ° (see computations in the Tab S6 [17]). **b** Composite diffraction images of the β-Sn phase at 9.1 GPa (left) and γ-Sn phase at 12.3 GPa (right), collected during the third cycle. Green, cyan and magenta square boxes indicate the positions of XRD peaks for β_C, γ_E and γ_F single crystals during the third cycle, respectively. Common diffracted peaks evidence the $(112)_\gamma$ twinning relation between the two variants of the same mechanism (see text). **c**,**d** Pole figures showing TW OR between β_C (empty black circles) and γ_E (cyan dots) and γ_F (magenta dots). In both cases, the observed OR present a misorientation of ~ 1. 5° compared to the perfect ones. Blue arrows highlight the coincidences. The identification of the plane and direction related to the mechanism are displayed for γ-Sn. Horizontal line is the compression direction.

herringbone microstructure composed of stacked γ-Sn twinned layers sharing $(112)_\gamma$ interfaces, as schematically illustrated in Fig. 4c. The size of these structures should be smaller than the X-ray beam (8 × 12 µm), as both orientations are systematically observed on each XRD image. The remaining 0.104 strain mainly consists of shear deformation, which could be facilitated by the low values of the C_{44} and C_{66} stiffness components for both phases. For β-Sn at ambient, C_{44}=22 GPa and C_{66}=24 GPa[23], and ab initio calculations predict that $C_{44} \simeq 11$ GPa in γ-Sn[24]. In addition, the orientation of $(112)_\gamma$ interfaces for $\gamma_E + \gamma_F$ or $\gamma_G + \gamma_H$ microstructures is roughly perpendicular to the sample surface, which also allows releasing shear stress by surface upheaval.

We observe that $\gamma \rightarrow \beta$ transformation exhibits a partially reconstructive character. How this interacts with the displacive mechanism chosen by the system for this transformation is explored below, with the help of time-resolved measurements.

Dynamic measurements

In separate experiments, powder samples of Sn are compressed and decompressed in the 1–20 GPa range, without a pressure-transmitting medium, and characterized with XRD in dynamic diamond anvil cells (dDAC) at 300 K. Compression rates vary between 20 and 150 GPa/ms (corresponding to strain rates of ~ 400–4000 s^{-1}), and XRD integration times are 10 μs (corresponding to a maximum pressure change of 1.5 GPa). A range of frequencies for XRD exposures is tested, which allows constraining the conditions of the $\beta \rightarrow \gamma \rightarrow \beta$ transformations at the 10 µs timescale and to monitor the evolution of the microstructures after the transformation at the ms timescale. See 'Methods' section for more details.

The direct β-Sn → γ-Sn transition proceeds at 11.0 GPa, with no effect of compression rate; this is in line with recent shock measurements where the transition pressure measured at 10^6 GPa/ms compression rate is found to agree with the static transition pressure[12,25]. From the similarity in XRD images, we infer that γ-Sn microstructure consists of powder grains with a size of the same order as starting β-Sn.

On the contrary, γ-Sn → β-Sn reversion condition exhibits a definite sensitivity to decompression rate. Fig. 5a shows a transition at $P_{dynamic}$=6.35 ± 0.7 GPa, the pressure corresponding to the single XRD frame where γ-Sn and β-Sn coexist. The uncertainty of 0.7 GPa corresponds to the pressure variation during XRD integration of 10 μ s for a decompression rate of -150 GPa/ms. This transition pressure is lower than P_{static}=9.4 ± 0.8 GPa, see Table S2. The difference $\Delta P = P_{static} - P_{dynamic}$ measured at various compression rates, including ref. 26, is plotted in Fig. 5b. The measured ΔP can be described by the phenomenological expression ($\dot{P} < 0$):

$$\Delta P = a \exp(b/\dot{P}) \ , \qquad (2)$$

with a = 4.46 GPa and b = 50.5 GPa/ms. Eq. (2) interpolates between two limits. As $\dot{P} \rightarrow 0$, the growth step has time to proceed and the reversion is detected at the static pressure. At high rate, decompression outruns growth, and ΔP saturates at a, the maximum metastability of γ -Sn, a value directly measured by the shock-release point of ref. 26. The parameter b is the characteristic decompression rate separating the two regimes.

The time-resolved XRD measurements also reveal an evolution of β-Sn microstructure at the ms time-scale. γ-Sn → β-Sn transition produces a fine powder of β-Sn, which immediately recrystallizes to form larger single-crystalline grains, producing intense XRD peaks on the two-dimensional detector as shown in Fig. 6a.

This evolution has been quantified using the relation between the average single crystal grain size G and the number of crystallites N_g contained in the irradiated volume V ($N_g \propto 1/G^3$). The relation can be extended to the number of (hkl) diffraction spots collected on the detector[27,28]; we focused here on the high multiplicity $(101)_\beta$ reflection. Diffraction patterns have been azimuthally unrolled, and the number of $(101)_\beta$ diffraction spots (N_{101}) has been measured within 150° azimuthal angle (Fig. 6a bottom); it decreases with time as shown in Fig. 6b. This trend has been fitted with a Burke normal grain growth law[29], relevant for high temperature grain growth kinetics:

$$G^n - G_0^n = kt \ , \qquad (3)$$

G_0 is the starting grain size, n = 2, and k is the growth constant. The fit result, with G_0 = 3.06 ± 0.05 µm and $k = 1.79 \pm 0.05 \times 10^{-15}$ $m^2/\mu s$, is also plotted in Fig. 6b (the uncertainties arise solely from the fitting procedure). This corresponds to an increase in grain size by a factor of 1.7 in 10 ms. Two different timescales are thus revealed by dynamic experiments: nucleation of β-Sn, within less than 22 µs (the time between two successive XRD frames), and its high-temperature recrystallization, with typical timescales of the order of 10 ms.

Discussion

The observations made under static and dynamic compression detail our view of β-Sn ↔ γ-Sn mechanisms at 300 K. A martensitic mechanism, either coupled with twinning or with a strong variant selection, explains the β-Sn → γ-Sn orientation relations measured in the static experiments. Martensitic transformations are fast, at the ns timescale[25], and dynamic

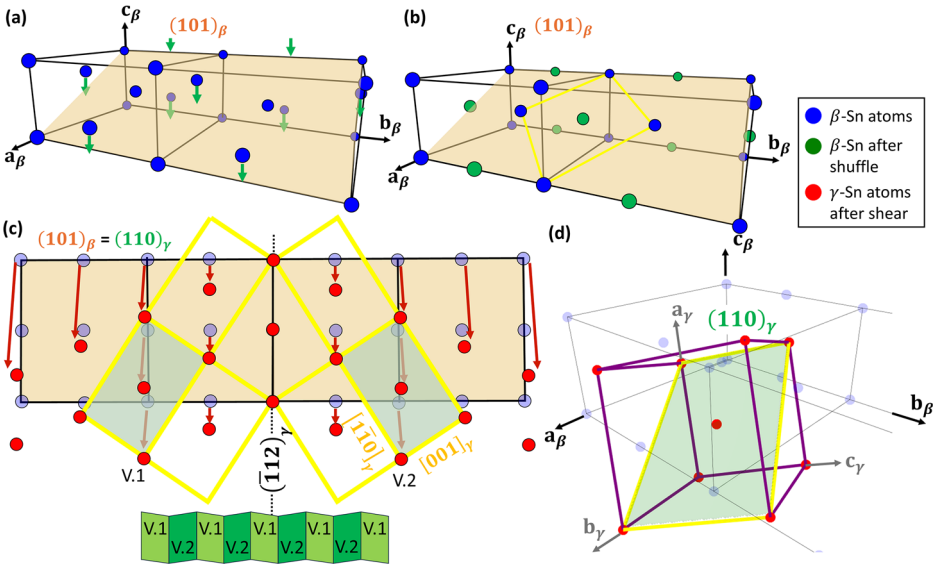


Fig. 4 | Schematic illustration of shuffle and shear associated with TW mechanism. a Shuffle: vertical translation (indicated with green arrows) of four atoms of the conventional unit cell; after shuffle **b**, a pattern matching $(110)_\gamma$ planes' configuration appears in $(101)_\beta$ planes (highlighted with yellow lines). Green atoms represent the atoms impacted by shuffle. **c** Shear in $(101)_\beta$ plane. Blue/red atoms are the position before/after applying F_1 strain (see section S.I [17]). Two variants V.1 and V.2 can be formed in a symmetric way to reduce the global shear (see text) and form the so-called herringbone microstructure, with $(\bar{1}12)_\gamma$ plane as interface. The yellow rectangle indicates $[1\bar{1}0]_\gamma$ and $[001]_\gamma$ directions. **d** Unit cell of γ-Sn (purple rectangular prism with red atoms) represented within β-Sn unit cell.

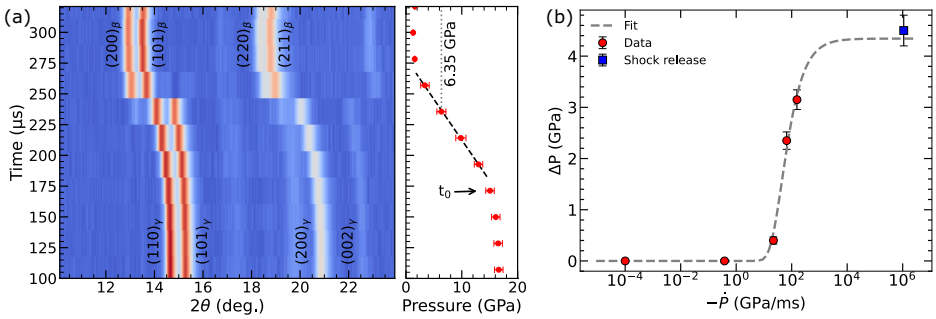


Fig. 5 | a Representative example of the γ-Sn → β-Sn phase transition measurement with time-resolved XRD under dynamic decompression, starting at t_0. Left: time evolution of the azimuthally integrated XRD signal. Each 10 μs exposure is followed by a 11.41 μs readout dead time, yielding one XRD pattern every 21.41 μs. In one spectrum at t_0+65 μs, P=6.35 ± 0.7 GPa, γ-Sn and β-Sn are seen to coexist. Right: pressure vs time. The black dashed line is a linear fit of decompression pressure, corresponding to a rate of -150 GPa/ms. Each pressure point is obtained from a single XRD pattern. Error bars represent the 1σ uncertainty propagated from the lattice-parameter refinement and the EoS of ref. 10. **b** $\Delta P = P_{static} - P_{dynamic}$, with $P_{static}/P_{dynamic}$ static/dynamic γ-Sn → β-Sn transition pressures *vs.* decompression rate $-\dot{P}$. Each red point corresponds to one independent experiment, with five independent experiments in total. Vertical error bars represent the uncertainty on ΔP propagated from the transition pressure determination. The shock release point and its error bars are taken from ref. 26. The gray-dashed lines is the best-fit results of Eq. (2), for which the shock release point was not included.

experiments show that β-Sn → γ-Sn transition conditions are insensitive to compression rate. β-Sn → γ-Sn thus exhibits a strong martensitic character.

On the contrary, dynamic γ-Sn → β-Sn reversion conditions are sensitive to decompression rate. The saturation of ΔP at a = 4.46 GPa, directly measured by the shock-release point of ref. 26, indicates that γ -Sn cannot be metastably preserved below $P_{static} - a \simeq 4.9$ GPa even at the highest decompression rates, while the static reversion pressure is 9.4 ± 0.8 GPa. Numerous β-Sn grains nucleate as small crystallites in less than a few μ s, as shown by the continuous β-Sn XRD rings collected in dynamic experiments. This event is followed by β-Sn single-crystal growth within a 10 ms timescale. This is in line with static decompression observations, where similar nucleation and growth steps are inferred for the γ-Sn → β-Sn transition from the final microstructure. The two platforms also differ in the density of potential heterogeneous nucleation sites: the dynamic samples are powders compressed without a pressure-transmitting medium, whereas the static ones are quasi-single crystals in helium. Since $P_{\beta\to\gamma}$ is the same in both cases, this difference does not measurably shift the direct transformation conditions. However, it does account for the different number of β -Sn nuclei formed upon reversion. Due to the smaller number of grains in the statically loaded samples and the proximity to the thermodynamic transition pressure, only a limited number of β-Sn grains are expected to form. In any case, they would grow or recrystallize at 10 ms timescale, forming a few healed single crystals. This explains the static formation of a few good-quality β-Sn single crystals and the scattered values of transition pressure (9.4 ± 0.8 GPa), the transition being triggered by the formation of one β-Sn nucleus. Nevertheless, the orientation relations repeatedly observed for the static reversion show that the nucleus is formed with a martensitic mechanism. Grain coarsening by recrystallization is likely to be promoted by residual stresses within the microstructure, which also advocates for a martensitic nucleation process. The kinetic description of γ-Sn → β-Sn transition requires taking into account its mixed diffusive/martensitic character.

Conclusion

In this work, we investigated the β-Sn ↔ γ-Sn transformations under pure hydrostatic compression at 300 K and analyzed the microstructures formed over multiple compression-decompression cycles. The effect of strain rate has also been studied in separate experiments. Different mechanisms are

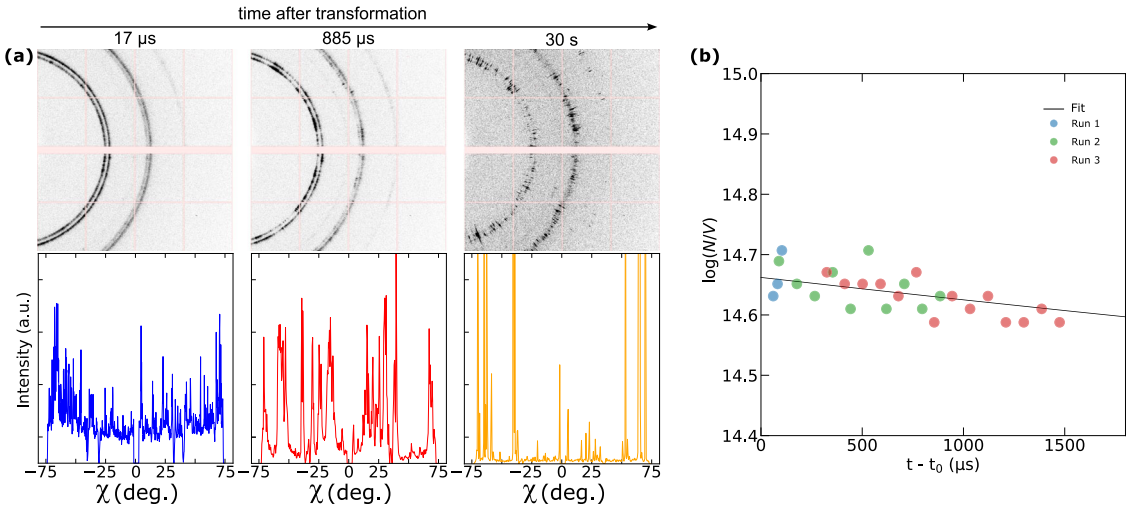


Fig. 6 | a XRD signal of β-Sn at ~ 1.5 GPa, after decompression at -150 GPa/ms. (bottom) One-dimensional patterns obtained by azimuthal projection of the intensity along the $(101)_\beta$ diffraction peak of the two-dimensional patterns. The number of peaks in bottom graphs corresponds to the number of peaks detected. **b** Time evolution of the volume-normalized number of grains N/V in β-Sn detected by XRD after phase transformation in the three different runs. The time indicated is the delay between the onset of decompression (t_0) and XRD collection; γ-Sn $\rightarrow$ β-Sn transformation is observed at ~ t_0 + 65 µs. The black line corresponds to a fit with Burke normal grain growth (see text).

disclosed for β-Sn $\rightarrow$ γ-Sn and γ-Sn $\rightarrow$ β-Sn transitions, that should be described with different kinetic laws.

The $\beta \rightarrow \gamma$ transformation is found to be martensitic. During the first transition, (101)[10-1] twinning in γ-Sn is activated, which appears to be a facilitating mechanism. For further transformation cycles, a specific OR, characterized by $(101)_\beta||(110)_\gamma$ and $[10\bar{1}]_\beta||[1\bar{1}1]_\gamma$, is consistently observed with the formation of two specific self-accommodating variants in γ-Sn, and the microstructure stabilizes. We propose that the transformation leads to the formation and accumulation of low-energy, highly compatible interfaces between selected variants at the μ m scale. These interfaces are likely reversible at low energetic cost. No strain rate effect on the transition pressure could be measured in the scanned range ($P_{\beta\rightarrow\gamma}$=10.9 ± 0.2 GPa from 10^{-2} to 4000 s^{-1}).

The $\gamma \rightarrow \beta$ reverse transition presents a diffusive character allowed by $T/T_{\text{Melting}} \sim 0.4$. Martensitic grain nucleation (attested by static TW OR) and subsequent grain growth (with typical time of 10 ms) steps could be distinguished with 22 µs-time-resolved measurements. Increasing the decompression rate to 4000 s^{-1} results in a decrease in the $\gamma \rightarrow \beta$ transition pressure, from 9.4 ± 0.8 GPa to 6.35 ± 0.7 GPa. We expect that γ-Sn cannot be preserved below 4.9 GPa, even for higher decompression rates.

Overall, the existence of an asymptotic transition pressure and the pronounced mediation by crystal-modifying processes (twinning, recrystallization, etc.) point toward the necessity of a coupled framework for transformation kinetics, not relying solely on a phenomenological viscosity parameter.

Methods

Two different types of Sn samples were studied during static experiments: powder grains (99.8% purity, Alfa Aesar) for Run 1 and a 15 µm-thick cold-rolled foil (99.95% purity, Goodfellow), annealed 2h at 450 K under vacuum for Run 2. A disc with a diameter of 80 μm was then cut in the foil with a femtosecond laser. As discussed and presented in Fig. 1, Run 1 powder grains turned out to be β-Sn single crystals, and a large part of Run 2 annealed foil was a β-Sn single crystal.

Samples were loaded in DAC equipped with diamonds with culets of 500/400 µm (Run 1/Run 2) together with a pressure gauge in a pre-indented rhenium gasket (see insets in Fig. 1). Almax-Boehler DAC design was used to ensure a wide angular opening in Run 2. Helium was used as a pressure transmitting medium (PTM), and we checked that the gap between the anvils remained larger than the sample thickness; we thus consider that the experiments have been carried out under hydrostatic pressurizing conditions[30,31]. Pressure was determined using the equation of state (EOS) of Gold[32] or NaCl[33]. Since these EOS parameters were proposed before the publication of the international practical pressure scale (IPPS-Ruby2020[34]), we modified the Rydberg-Vinet EOS parameters to take into account this new calibration: for Au, K_0 = 161.9 GPa, K'_0 = 6.1 and V_0 = 67.95Å^3/atom; for B1-NaCl, K_0 = 23.5 GPa, K'_0 = 5.5 and V_0 = 44.90Å^3/atom[35].

Experiments were carried out at the PSICHE beamline of SOLEIL synchrotron (France). Angular dispersive X-ray diffraction (XRD) data were collected on a CdTe 2M PILATUS detector, using a monochromatic (0.3738 Å) X-ray beam with a 8×12 µm^2 full width at half maximum (FWHM) spot on the sample. The sample-to-detector distance, calibrated using a reference CeO_2 sample, was around 370 mm.

The DAC was rotated between $-\theta_{max}$ and $+\theta_{max}$ around a vertical axis and one XRD pattern was collected within θ_{step} (see details in Tab. S4, Fig. S6). In total, $2\theta_{max}/\theta_{step}$ XRD spectra were recorded for these multi-exposure datasets. In Run 2, XRD mapping was also performed throughout the sample using a 50×50 µm^2 grid (25 points) to check homogeneity of its microstructure at selected pressure steps.

The bidimensional images were integrated using Dioptas software[36] to identify phases. Then multiexposure XRD data were processed in order to determine the crystalline orientation of the grains in the sample. TIMELeSS multigrain tools, available from the FABLE project(https://github.com/FABLE-3DXRD/TIMEleSS) are dedicated to this purpose for DAC experiments. For indexation, Grainspotter[37] was used, as in several studies in the literature[18,38,39]. The different grain orientations were exported as Euler angles with a Bunge convention[40]. All Euler angles obtained during this work are available in the Supplementary[17] (Tab. S3). Lattice planes and directions are plotted in pole figures (as presented in several figures in this report) using MTEX toolbox[41] to determine possible OR between phases.

Dynamic compression experiments were performed using a modification of a membrane-DAC[42] with a piston guided by four rods, in conjunction with the Piezosystem Jena HPST 1000/35-25/80 VS45 to apply the force on the piston. A waveform Tabor Electronics WW2074 and an Amplifier Piezosystem Jena RCV 1000/7 are used to deliver the current in the piezoactuator with a chosen profile. This system was synchronized with XRD on ID09 bbeamlineat ESRF, where a 19 keV quasi-monochromatic beam (spot size ~ 25 μm FWHM) was used ($\Delta E/E$ = 2%[43]). A JUNGFRAU 1M detector was used to collect the XRD signal, operating at up to 250 kHz frame rates, with typical 10 μ s exposure times. The set-up for piezoelectric

actuator dDAC assemblies was as described in ref. 44–49. The fine control of pre-pressurization allows producing both compression and decompression ramps in the typical range 2–50 GPa, 20–200 GPa/ms, with highly reproducible P vs t paths. The same driving signal was applied to the piezoelectric actuator in successive runs while probing the sample at distinct times, monitoring the β-Sn ↔ γ-Sn transformations at various compression/decompression rates.

DACs were equipped with an LMAX-Boehler design DAC with 300 μ m culets. Stainless steel gaskets were used for all experiments, indented to 40 μ m thickness with a 100 μm-diameter hole for the experimental chamber. Sn powder samples with typical grain sizes of a few microns were loaded without a pressure-transmitting medium. Pressure was determined using Sn azimuthally integrated XRD signal and EOS of β-Sn and γ-Sn from ref. 10.

Data availability

Data available on reasonable request from the corresponding author. The raw data for the dynamic experiment can be found at https://doi.org/10.15151/ESRF-ES-1126485618

Received: 13 May 2026; Accepted: 8 October 2026;
Published online: 14 November 2026

References

1. Smith, R. F. et al. Time-dependence of the alpha to epsilon phase transformation in iron. *J. Appl. Phys.* **114**, 223507 (2013).
2. Jeneiv, Z. S. et al. New dynamic diamond anvil cells for tera-pascal per second fast compression x-ray diffraction experiments. *Rev. Sci. Instrum.* **90**, 065114 (2019).
3. Tang, M. et al. In situ X-ray diffraction of the α−ε phase transition in iron at intermediate strain rates. *Phys. Rev. Res.* **8**, 013135 (2026).
4. Chen, X. et al. Kinetic control of high-pressure phase transitions in anatase tio$_2$. *Phys. Rev. B* **111**, 104108 (2025).
5. Ocampo, I. K. et al. Ultrafast x-ray diffraction of high-pressure phases in dynamically compressed tio$_2$. *Phys. Rev. B* **112**, 104103 (2025).
6. Coleman, A. L. et al. Identification of phase transitions and metastability in dynamically compressed antimony using ultrafast x-ray diffraction. *Phys. Rev. Lett.* **122**, 255704 (2019).
7. McBride, E. E. & Krygier, A. et al. Phase transition lowering in dynamically compressed silicon. *Nat. Phys.* **15**, 89–94 (2019).
8. Pépin, C. M. et al. Kinetics and structural changes in dynamically compressed bismuth. *Phys. Rev. B* **100**, 060101 (2019).
9. Salamat, A. et al. Dense close-packed phase of tin above 157 GPa observed experimentally via angle-dispersive X-ray diffraction. *Phys. Rev. B* **84**, 140104 (2011).
10. Salamat, A. et al. High-pressure structural transformations of Sn up to 138 GPa: angle-dispersive synchrotron x-ray diffraction study. *Phys. Rev. B* **88**, 104104 (2013).
11. Briggs, R. et al. Observation of the shock-induced β-Sn to b.c.t.-Sn transition using time-resolved X-ray diffraction. *J. Synchrotron Radiat.* **26**, 96–101 (2019).
12. Fréville, R. et al. High-pressure–high-temperature phase diagram of tin. *Phys. Rev. B* **109**, 104116 (2024).
13. Katzke, H., Bismayer, U. & Tolédano, P. Theory of the high-pressure structural phase transitions in Si, Ge, Sn, and Pb. *Phys. Rev. B* **73**, 134105 (2006).
14. Musgrave, M. J. P. On the transition from white tin (β-sn) to the body-centred cubic form under pressure. *J. Phys. Chem. Solids* **24**, 557–558 (1963).
15. Nishiyama, Z. *Martensitic transformation*. (Elsevier, 2012).
16. Christian, J. W. & Mahajan, S. Deformation twinning. *Prog. Mater. Sci.* **39**, 1–157 (1995).
17. See supplemental material at [url will be inserted by publisher] that includes: (i) notation for twinning elements; (ii) precise conditions of the transformation and EoS; (iii) the crystal quality evolution with cycles; (iv) table of Euler angles determined in this work; (v) a schematic of the diffraction setup; and details about the mechanism: (vi) variants created; (vii) comparison using Vigilano software; and (viii) appendix for computation of the transformation strain. Contains Refs. [10, 12, 16, 32, 33, 45-48].
18. Fréville, R., Dewaele, A., Bruzy, N., Svitlyk, V. & Garbarino, G. Comparison between mechanisms and microstructures of α−γ, γ−ϵ, and α−ϵ−α phase transitions in iron. *Phys. Rev. B* **107**, 104105 (2023).
19. Aaronson, H. I. Mechanisms of the massive transformation. *Metall. Mat. Trans. A* **33A**, 2285 (2002).
20. Bruzy, N., Druette, L., Médrala, C., Barraud, É & Denoual, C. Identification of diffusionless transformation sequences from crystal orientation data. *Mater. Today Commun.* **46**, 112641 (2025).
21. Hawreliak, J. A. & Turneaure, S. J. Observations of twinning microstructure in iron ramp-compressed through the α − ϵ phase transition. *Phys. Rev. B* **106**, 174306 (2022).
22. K.Bhattacharya. Microstructure of martensite: why it forms and how it gives rise to the shape-memory effect, vol. 2. (Oxford University Press, 2003).
23. Rayne, J. A. & Chandrasekhar, B. S. Elastic Constants of β Tin from 4.2°K to 300°K. *Phys. Rev.* **120**, 1658–1663 (1960).
24. Nitol, M. S. et al. Hybrid interatomic potential for Sn. *Phys. Rev. Mater.* **7**, 043601 (2023).
25. Threadingham, J. G. et al. Effects of crystal orientation on the shock properties of single crystal tin. *J. Appl. Phys.* **139**, 065902 (2026).
26. Sollier, A. et al. Development of a laser-driven shock compression platform for time-resolved XRD experiments at the ID09 beamline of the european synchrotron radiation facility. *High. Press. Res.* **44**, 418–441 (2024).
27. Kubo, T. et al. Time-resolved two-dimensional x-ray diffraction measurements of kinetic properties in polycrystalline high-pressure ices. *J. Phys. Conf. Ser.* **215**, 012022 (2010).
28. Yamazaki, D. et al. Grain growth of ϵ-iron: Implications to grain size and its evolution in the Earth's inner core. *Earth Planet. Sci. Lett.* **459**, 238–243 (2017).
29. Burke, J. E. The fundamentals of recrystallization and grain growth. Grain Control in Industrial Metallurgy, 1–73 (Springer, 1949).
30. Dewaele, A. & Loubeyre, P. Pressurizing conditions in helium-pressure-transmitting medium. *High. Press. Res.* **27**, 419–429 (2007).
31. Klotz, S., Chervin, J.-C., Munsch, P. & Le Marchand, G. Hydrostatic limits of 11 pressure transmitting media. *J. Phys. D Appl. Phys.* **42**, 075413 (2009).
32. Takemura, K. & Dewaele, A. Isothermal equation of state for gold with a He-pressure medium. *Phys. Rev. B* **78**, 104119 (2008).
33. Dewaele, A. Equations of State of Simple Solids (Including Pb, NaCl and LiF) Compressed in Helium or Neon in the Mbar Range. *Minerals* **9**, 1–8 (2019).
34. Shen, G. et al. Toward an international practical pressure scale: a proposal for an IPPS ruby gauge (IPPSRuby2020). *High. Press. Res.* **40**, 299–314 (2020).
35. R.Fréville. *Transitions de phase et microstructures induites dans les métaux en conditions extrêmes : fer et étain*. Theses, (Université Paris-Saclay, 2023).
36. Prescher, C. & Prakapenka, V. B. DIOPTAS: a program for reduction of two-dimensional X-ray diffraction data and data exploration. *High. Press. Res.* **35**, 223–230 (2015).
37. Schmidt, S. GrainSpotter: a fast and robust polycrystalline indexing algorithm. *J. Appl. Crystallogr.* **47**, 276–284 (2014).
38. Dorothea Rosa, A. et al. In situ monitoring of phase transformation microstructures at Earth's mantle pressure and temperature using multi-grain XRD. *J. Appl. Crystallogr.* **48**, 1346–1354 (2015).
39. Langrand, C. et al. Reliability of multigrain indexing for orthorhombic polycrystals above 1 Mbar: application to MgSiO3 post-perovskite. *J. Appl. Crystallogr.* **50**, 120–130 (2017).

40. H.-J.Bunge. Texture analysis in materials science. In H.-J. Bunge, editor, Texture Analysis in Materials Science, pp. 3–41 (Butterworth-Heinemann, 1982).
41. Bachmann, F., Hielscher, R. & Schaeben, H. Grain detection from 2D and 3D EBSD data-specification of the MTEX algorithm. *Ultramicroscopy* **111**, 1720–1733 (2011).
42. Letoullec, R., Pinceaux, J. P. & Loubeyre, P. The membrane diamond anvil cell: a new device for generating continuous pressure and temperature variations. *High. Press. Res.* **1**, 77–90 (1988).
43. Levantino, M. et al. Structural dynamics probed by X-ray pulses from synchrotrons and XFELs. *Comptes Rendus. Phys.* **22**, 75–94 (2021).
44. Pépin, C. M. et al. Metastable water at several compression rates and its freezing kinetics into ice vii. *Nat. Commun.* **15**, 8239 (2024).
45. Lehman, L. P., Xing, Y., Bieler, T. R. & Cotts, E. J. Cyclic twin nucleation in tin-based solder alloys. *Acta Materialia* **58**, 3546–3556 (2010).
46. Tu, K. N. & Turnbull, D. Direct observation of twinning in lamellae. *Acta Metall.* **18**, 915–& (1970).
47. Boukouvala, C. et al. Beyond simple crystal systems: identifying twinning in bodycentered tetragonal nanoparticles. *Cryst. Growth Des.* **22**, 653–660 (2022).
48. Liu, T., Liang, L., Raabe, D. & Dai, L. The martensitic transition pathway in steel. *J. Mater. Sci. Technol.* **134**, 244–253 (2023).
49. L.Druette, N.Bruzy, and R.Lemaire. Vigilano. https://gitlab.com/vigilano/vigilano.git (2025).

Acknowledgements

The authors would like to thank Christophe Denoual for fruitful discussions on the transformation mechanism. We thank Paul Chauvigné and Laura Henry for their help with the experiments. The static experiments have been performed at Soleil during proposals 20221716 and 20240361 (BAG handled by Y. LeGodec). The authors acknowledge the European Synchrotron Radiation Facility for provision of synchrotron radiation facilities on beamline ID09 for the dynamic experiments, during beam time HC-5293.

Author contributions

A.D. proposed the research. R.F., A.D., N.B., and N.G. conducted the static experiment. C.P., F.O., and M.L. conducted the dynamic experiment. R.F. and C.P. processed and analyzed the data. N.B. performed the Vigilano computations. All authors discussed the interpretation of results and reviewed the manuscript.

Funding

The authors received no specific funding for this work.

Competing interests

The authors declare that they have no known competing financial interests or personal relationships that could have appeared to influence the work reported in this paper.

Additional information

Supplementary information The online version contains supplementary material available at https://doi.org/10.1038/s43246-026-01418-0.

Correspondence and requests for materials should be addressed to Robin Fréville.

Peer review information : *Communications Materials* thanks Chuanlong Lin and the other, anonymous, reviewer(s) for their contribution to the peer review of this work. A peer review file is available.

Reprints and permissions information is available at http://www.nature.com/reprints

Publisher's note Springer Nature remains neutral with regard to jurisdictional claims in published maps and institutional affiliations.

Open Access This article is licensed under a Creative Commons Attribution 4.0 International License, which permits use, sharing, adaptation, distribution and reproduction in any medium or format, as long as you give appropriate credit to the original author(s) and the source, provide a link to the Creative Commons licence, and indicate if changes were made. The images or other third party material in this article are included in the article's Creative Commons licence, unless indicated otherwise in a credit line to the material. If material is not included in the article's Creative Commons licence and your intended use is not permitted by statutory regulation or exceeds the permitted use, you will need to obtain permission directly from the copyright holder. To view a copy of this licence, visit http://creativecommons.org/licenses/by/4.0/.

© The Author(s) 2026

This Article in Press is shared early to give you faster access to new research. It is citable and carries a permanent DOI. The final edited version will replace it automatically.